



An efficient retinal blood vessel segmentation in eye fundus images by using optimized top-hat and homomorphic filtering

Oscar Ramos-Soto^a, Erick Rodríguez-Esparza^{a,b}, Sandra E. Balderas-Mata^a, Diego Oliva^{a,c,*}, Aboul Ella Hassanien^d, Ratheesh K. Meleppat^{e,f}, Robert J. Zawadzki^{e,f}

^a División de Electrónica y Computación, Universidad de Guadalajara, CUCEI, Av. Revolución 1500, C.P. 44430, Guadalajara, Jal., Mexico

^b DeustoTech, Faculty of Engineering, University of Deusto, Av. Universidades, 24, 48007 Bilbao, Spain

^c IN3 - Computer Science Dept., Universitat Oberta de Catalunya, Castelldefels, Spain

^d Faculty of Computers and AI, Cairo University, Giza, Egypt

^e UC Davis Eyepod Imaging Laboratory, Dept. of Cell Biology and Human Anatomy, University of California Davis, Davis, CA 95616, USA

^f Dept. of Ophthalmology & Vision Science, University of California Davis, Sacramento, CA, USA

ARTICLE INFO

Article history:

Received 14 September 2020

Accepted 18 January 2021

Keywords:

Retinal blood vessel segmentation

Optimized top-hat

Homomorphic filtering

MCET-HHO algorithm

ABSTRACT

Background and objective: Automatic segmentation of retinal blood vessels makes a major contribution in CADx of various ophthalmic and cardiovascular diseases. A procedure to segment thin and thick retinal vessels is essential for medical analysis and diagnosis of related diseases. In this article, a novel methodology for robust vessel segmentation is proposed, handling the existing challenges presented in the literature.

Methods: The proposed methodology consists of three stages, pre-processing, main processing, and post-processing. The first stage consists of applying filters for image smoothing. The main processing stage is divided into two configurations, the first to segment thick vessels through the new optimized top-hat, homomorphic filtering, and median filter. Then, the second configuration is used to segment thin vessels using the proposed optimized top-hat, homomorphic filtering, matched filter, and segmentation using the MCET-HHO multilevel algorithm. Finally, morphological image operations are carried out in the post-processing stage.

Results: The proposed approach was assessed by using two publicly available databases (DRIVE and STARE) through three performance metrics: specificity, sensitivity, and accuracy. Analyzing the obtained results, an average of 0.9860, 0.7578 and 0.9667 were respectively achieved for DRIVE dataset and 0.9836, 0.7474 and 0.9580 for STARE dataset.

Conclusions: The numerical results obtained by the proposed technique, achieve competitive average values with the up-to-date techniques. The proposed approach outperform all leading unsupervised methods discussed in terms of specificity and accuracy. In addition, it outperforms most of the state-of-the-art supervised methods without the computational cost associated with these algorithms. Detailed visual analysis has shown that a more precise segmentation of thin vessels was possible with the proposed approach when compared with other procedures.

© 2021 Elsevier B.V. All rights reserved.

* Corresponding author.

E-mail addresses: oscar.ramos9279@alumnos.udg.mx (O. Ramos-Soto), erick.rodriguez@deusto.es (E. Rodríguez-Esparza), sandra.balderas@academicos.udg.mx (S.E. Balderas-Mata), diego.oliva@cucei.udg.mx (D. Oliva), aboitcairo@fci-cu.edu.eg (A.E. Hassanien), rkmeleppat@ucdavis.edu (R.K. Meleppat), rjzawadzki@ucdavis.edu (R.J. Zawadzki).

1. Introduction

The eye fundus examination is widely used for ophtalmologist and other physicians as a common clinical test for the prevention, diagnosis, and monitoring treatment of ocular diseases such as retinal thrombosis, glaucoma, senile maculopathy, among others [1]. The eye fundus exam constitutes a color imaging technique of the retinal surface of the human eye, in which the main anatomical structures (optic disc, macula, and vascular tree) can be examined [2].

Segmentation of the retinal vascular tree has great relevance in the field of medical imaging, due to the fact that the **retina is the only part of the human body which is possible to observe blood microcirculation through a non-invasive method for the detection of systematic diseases such as hypertension**, diabetes, arteriosclerosis, liver diseases, to name just a few [3–5]. Through the segmentation of the retinal vessels, morphological information like size, length, width, branching, and angles of retinal vasculature can be measured [6]. Performing this segmentation manually becomes a time-consuming task that requires knowledge and experience from medical experts [7]. Furthermore, subjective perception can lead to a non-consistent segmentation due to experts may not use the same pixel classification criteria [8–10].

Therefore, developments and implementation of automated methods for robust vessel extraction are essential in Computer-Aided Diagnosis (CADx) for early diagnosis and evaluation of a disorder with the objective of reducing medical costs and improve efficiency [11,12]. However, there are several challenges in segmentation; the first one is due to other optical elements in the eye fundus, such as the optic disk, the macula, and artifacts generated by pathologies, which hinder the automatic segmentation of the vessels. The second one arises due to the diversity of the vessel width and the low contrast presented by the thin vessels in comparison with the background. Finally, the third challenge is caused by the diversity of the shape, size, and intensity of the vessel pixels that difficult the correct segmentation [5,13,14].

Over the past decades, several methods for the automated segmentation of the retinal vessels using the fundus examination have been widely used, this task continues to be of great interest to the scientific community due to increasingly accurate results [15]. Overall, the previously proposed algorithms are classified into supervised and unsupervised methods. Supervised approaches use a group of samples to train a classifier that discriminates between the vessel and non-vessel pixels to build an optimal predictive model, the set used in this kind of method is called training set. These methods are subsequently classified into machine learning and deep learning algorithms. Machine learning techniques mainly consist of three stages: the first one is the extraction of features from pixels [16–18], the second is the selection of features [19–21], and finally, the classification of the extracted vectors in the corresponding labels [22–25]. In image classifications in the medical area, several feature extractors have been proposed such as bag-of-visual-words [26], the Gaussian filter [27], the Gabor filter [28], to name a few. Moreover, some classifiers have been used, such as K-Nearest Neighbors (K-NN) [29], Random Forest [30], Support Vector Machine (SVM) [31], Artificial Neural Networks (ANN) [32], among others. Deep learning techniques overcome the problems of the traditional algorithms mentioned above because these approaches have the ability to exploit raw data without using handcrafted features through an automatic feature extractor [33,34]. These supervised methods produce satisfactory results for the extraction of healthy retinal vasculature [35,36]. However, a very important limitation of these methods is that the images need to present a ground-truth, which in practice represents information that is not so easy to acquire. Furthermore, machine learning and deep learning algorithms require a training process that is time-consuming and computationally expensive to satisfactorily complete the task in a new set of images [9].

On the other hand, unsupervised methods are systems that performance an image segmentation process without requiring a training data set. These methods are based on image processing: the first step pass the image through enhancement process, which is usually based on morphological image operations [37], matched filter responses [38], the complex continuous wavelet transform [39], adaptive histogram equalization [40], Hessian based filters [41–43], among others. The second step is to segment using mul-

tilevel thresholding [44–48] or region-oriented techniques, like region growing [49,50] or active contours [51,52]. These traditional unsupervised methods are primarily based on manual feature extraction for the representation and segmentation of the image elements. Mostly, the efficiency of the supervised methods is better than the unsupervised ones, also producing better results [11]. However, unsupervised systems are characterized by having the main advantage of performing the vessel segmentation process without prior knowledge of the ground-truth, which gives superiority to data sets without the labeling information of the pixels [13]. Furthermore, these methods are computationally less expensive and obtain results in a reduced amount of time. In recent years, both kind of methodologies (supervised and unsupervised) have been used, demonstrating good performance for retinal vessel segmentation. Nevertheless, the challenge of segmenting thin vessels still remains a limiting factor for the optimal performance of most of the works presented in the literature. These thin vasculature provide information of great importance in the detection of neovascular diseases [14]. Therefore, being able to achieve a better segmentation of these vessels is crucial for the detection and diagnosis of eye diseases [53].

This article introduces an accurate methodology for retinal vasculature segmentation to address most of the challenges mentioned above for retinal vessel segmentation on eye fundus image. The proposed approach is divided into three phases, namely, 1) pre-processing, 2) main processing, and 3) post-processing. In the first phase, a Gaussian filter is applied to obtain a smoothed gray-scale image of the fundus. The main processing phase is divided into two configurations. The first to segment thick vessels by applying a combination of filters (Optimized top-hat, Homomorphic, and Median), while the second configuration to segment thin vessels by applying a combination of filters (Optimized top-hat, Homomorphic, and Matched) and multilevel segmentation through the Multilevel Cross-Entropy Harris Hawk Optimizer (MCET-HHO). Finally, morphological image processing is applied for the post-processing phase. Several experiments have been performed in two databases; the first one is called Digital Retinal Images for Vessel Extraction (DRIVE) [54] and the second one is the Structured Analysis of the Retina (STARE) [55], both publicly available online. Such databases are used to assess the performance of this methodology. The obtained results of the performance metrics demonstrate the advantages of the method, achieving closer or higher values compared to most of the up-to-date techniques, which have a greater computational complexity for retinal vessels segmentation.

The proposed approach presents an optimized top-hat transformation that includes the use of a segmentation step based on the MCET-HHO for thin vessel segmentation. Other techniques using the MCET-HHO algorithm have been previously proposed to segment medical images [56,57]. The main difference lies in that these studies are used to identify regions containing malignant masses in digital mammograms and also to compare the behavior of segmentation using different levels of applied thresholds.

The most important contributions of this article are summarized as follows:

- A novel methodology is proposed for thin and thick retinal blood vessel segmentation.
- A new variant of the classical top-hat operation is presented as the optimized top-hat.
- The variation of parameters of the optimized top-hat filter and the homomorphic filter depending on whether it is to segment thin or thick vessels.
- An automated method for robust retinal vessel segmentation for CADx tools.
- A minimum amount of false positives are obtained through this proposal.

- This approach overcomes the most recent unsupervised methods in terms of specificity and accuracy and competes with supervised methods but with a low computational cost.

The remainder paper is structured as follows: [Section 2](#) reviews the most recent methods of retinal blood vessel tree segmentation. In [Section 3](#), it is described the hybridization of the proposed method. [Section 4](#) presents the results and discussions of the paper. Finally, in [Section 5](#) the conclusions and further work are included.

2. Related work

As was mentioned in the previous section, there are many related papers in the state-of-the-art on retinal vascular tree segmentation in fundus images that fall into a general classification: supervised and unsupervised. Significant works for retinal vessel segmentation are briefly described below, against which the proposed methodology is compared to.

The lately published state-of-the-art unsupervised methods will be discussed here, for example in 2019, Wang et al. [58] proposed some modifications of the top-hat and bottom-hat transformations to give the images an enhancement by eliminating disturbances and noise, then for segmentation process, they used a novel technique called flattening of minimum circumscribed ellipse to recognize a vessel. Later, in the same year, Diaz et al. [59] suggested the use of the Lateral Inhibition technique (LI) to improve the contrast between the fundus and the retinal vessels. While for vessel segmentation, they applied the minimization of cross-entropy through the differential evolution (DE) algorithm to find the optimal value to efficiently segment vessels. In 2020, Shukla et al. [60] presented a new fractional filter to remove artifacts in the input image through a fractional mask that discards noise and preserves the edges of the thin vessels. Then, they obtained the pixels of the central line with their proposed algorithm and applied the Principal Component Analysis (PCA) to evaluate the first and different maps of the eigenvalues of the resultant image. Subsequently, they implemented the region growing operation with the objective to relate the pixels of the same vessel and apply the locate thresholding to segment the vessels. Later in 2020, Dos Santos et al. [61] used the Contrast Limited Adaptive Histogram Equalization (CLAHE) to increase the image contrast and reduce the existing noise in the fundus images using the Wiener filter. To establish the fixed configuration of the parameters of these filters, an Artificial Neural Network (ANN) is used to optimize and find the parameters combination that will present the best results. After that, Zhou et al. [62] proposed an improved line detector to extract the main structure of the vessels to subsequently apply the Hidden Markov Model (HMM) to effectively detect the lines of the central thin vessels. Finally, Pachade et al. [63] suggested a novel configuration for the segmentation, first enhance the contrast of the vessels, then apply a 2D median linear filter, to subsequently apply a combination of morphological image operations, background estimation, and an iterative threshold to complete the segmentation.

On the other hand, the most recent works on supervised methods will be briefly discussed, in 2019, Adapa et al. [64] published a supervised approach in which they first did a pre-processing that consists of the enhancement of the image using CLAHE filter to enhance the local contrast, followed by top-hat transform, then the extraction of features is made by using the Zernike moment for its subsequent binary classification through an ANN. Meanwhile, Yang et al. [65] presented an article in which the K-Singular Value Decomposition (K-SVD) is used to obtain multiple complementary features by using six different enhancement algorithms. However, in the training stage of its proposed method, the manually annotated ground-truth is needed to be able to classify vessels into

thin or thick vessels as the labeled data by using the K-SVD algorithm to train the dictionary for the vessel segmentation. Jin et al. [66] proposed the use of the Deformable U-Net (DUNet), to create a deep learning model to complete the segmentation. This model is a hybridization of the traditional U-Net and the Deformable Convolutional Network (Deformable-ConvNet). Later in 2020, Cheng et al. [67] presented using a new U-Net architecture made specifically for retinal vessel segmentation by adding a dense block to the network configuration, improving accuracy for both thin and thick vessels. Finally, Wu et al. [68] offered a novel configuration called NFN+, to build an efficient segmentation model, consisting of two cascading backbones, linked by inter-network skip connections. The function of the front network is to image patches and produce probability maps of the prime vessels, while the followed network takes the probability maps of the front network and generates refined results that are averaged to do the segmentation.

Supervised approaches learn from a model to be able to predict whether a pixel belongs to a category or not, which makes them somewhat superior in performance compared to unsupervised approaches. However, there are unsupervised models such as those presented above and the proposed in this article that obtain similar or even better results with less computational cost and time.

3. Methodology

This section briefly details the proposed algorithm, which is summarized in the flowchart shown in [Figure 1](#). The most important concepts used in the proposed methodology are presented here. The eye fundus image shows thick and thin blood vessels, the latter being unsegmented by most of the formerly proposed algorithms. The goal of this method is to segment thick and thin vessels and thus generate two images separately to later splice both resultant images and obtain a final segmentation result. To provide a better reference of the steps of the proposed algorithm, in [Figure 2](#), the output of the most important steps is shown.

3.1. Image pre-processing

Before performing the stages of thick and thin vessels processing, it is important to apply pre-processing stage over a retinal eye fundus image ([Figure 2 a](#)), which directly and positively influences the results. This task consists of two stages: **image green channel extraction** and the use of a **two-dimensional Gaussian filter**.

3.1.1. Green channel extraction

The **original** eye fundus image is provided in **RGB format**, which means that it is a **24-bit image**, therefore **each channel** (red, green and, blue) is **8 bits each**. Then the input can be considered as a three-layer image, and can be expressed as follows:

$$\mathbf{I} = [\mathbf{I}_{Rch} \ \mathbf{I}_{Gch} \ \mathbf{I}_{Bch}] \quad (1)$$

where \mathbf{I} is the input RGB image and \mathbf{I}_{Rch} , \mathbf{I}_{Gch} and \mathbf{I}_{Bch} represents the red, green and blue channels, represented by its layers. By performing an analysis of each separate channel, \mathbf{I}_{Gch} shows a great vessel-background contrast, while the \mathbf{I}_{Rch} and \mathbf{I}_{Bch} feature a higher amount of noise and considerable low contrast [69]. In addition, the vision of the human eye presents a superior response in green channel visual perception, compared to both green and red channels [70]. Accordingly, \mathbf{I}_{Gch} is taken out as a gray-scale image.

3.1.2. Gaussian filtering

Even though green-channel of eye fundus image shows a good vessel-background contrast regarding the RGB input image, it is positive and productive to use a noise removal step before consequent stages are performed. Gaussian smoothing filtering algorithm comes in handy in order to enhance image structures such

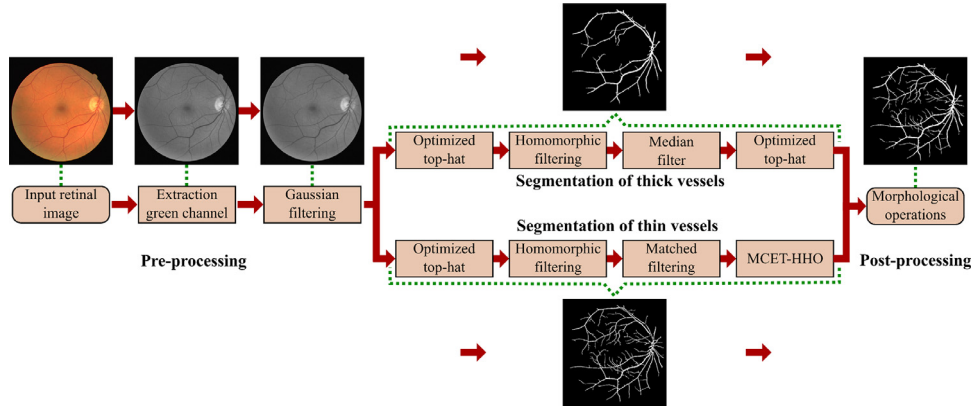


Fig. 1. Flowchart of the proposed method for vessel segmentation

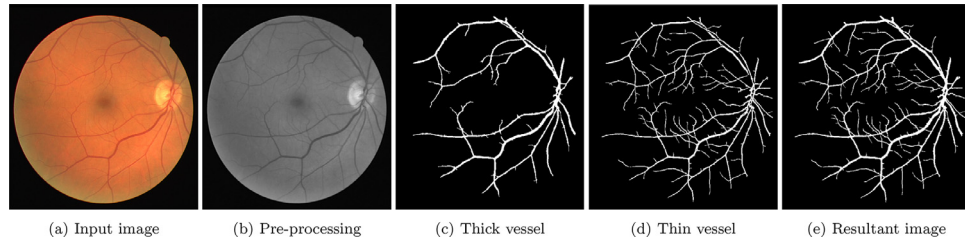


Fig. 2. Variations of top-hat algorithms

as previously contrasted elements. This type of filtering employs a Gaussian function (based on the so-called normal distribution widely used in statistics) to calculate the transformation by applying it to each pixel of the two-dimensional set. A Gaussian filtering representation $G(x, y)$ of an image is derived by the convolution of the input image $I_{Gch}(x, y)$ and the two-dimensional Gaussian kernel $g(x, y)$, the latter mathematically represented [71] as:

$$g(x, y) = \frac{1}{2\pi\sigma^2} \exp\left(-\frac{x^2 + y^2}{2\sigma^2}\right) \quad (2)$$

Therefore, $G(x, y)$ is determined as:

$$G(x, y) = g(x, y) * I_{Gch}(x, y) \quad (3)$$

where σ^2 is the variance of the Gaussian filter. Let $t = \sigma^2$ denote a scale parameter.

If the variance value approach to zero (hence $t = 0$) the filter behaves as an impulse function response, as expressed in the following equation:

$$G(x, y) = I_{Gch}(x, y) \quad (4)$$

As t increases the smoothing effect begins to accentuate more. In this filter, the standard deviation is defined as $\sigma = \sqrt{t}$, image details that are considerably smaller than this value are completely removed. After perform different experiments, the value of the variance is set as 0.463. The pre-processing stage result is displayed in Figure 2 b.

3.2. Segmentation of thick vessels

As seen in the Figure 1, the thick vessel segmentation process involves four stages, which are detailed below.

3.2.1. Optimized Top-hat

Morphological image operations are a powerful tool for image processing, the mathematical morphology is composed of algebraic

arithmetic operators that are applied to a gray-scale 2-D eye fundus image. The top-hat morphological operation is represented by the difference between the input image and its morphologically closed-form, it represents the interaction between the image and a structuring element of determined size and shape [72] and it is used to enhance bright objects of interest in a dark background, such as bright blood vessels obtained from a image complement (a concept which is defined below) of green channel image where the background turns dark. Let \mathbf{I} denote a gray-scale 2-D image and \mathbf{S}_0 the structuring element, the top-hat is defined in the following equation:

$$\mathbf{T}_{\text{HAT}}(\mathbf{I}) = \mathbf{I} - (\mathbf{I} \circ \mathbf{S}_0) \quad (5)$$

where (\circ) denotes the opening operator.

Different variations of modified top-hat were introduced by Salembier et al. [73] and their application to blood vessel segmentation have been previously done by Mendonça et al. [74] and BahadarKhan et al. [75]. In the methodology, it is proposed a new optimized top-hat technique that overcomes some problems presented by using the classical top-hat operation, which are detailed in the previously mentioned works. One of these drawbacks is that small intensity fluctuations have not been detected (which provide information about thin vessels). For this method proposal, the top-hat operator is applied to a complement image before the modified top-hat as well as the morphological image operations are inverted. The proposed optimized top-hat is defined as follows:

$$\mathbf{T}_0 = \mathbf{I}^c - (\mathbf{I}^c \circ \mathbf{S}_0) \bullet \mathbf{S}_c \quad (6)$$

where \mathbf{S}_0 and \mathbf{S}_c are the structuring elements for opening (\circ) and closing (\bullet) operators respectively and \mathbf{I}^c is the image complement of \mathbf{I} , defined as follows:

$$\mathbf{I}^c = \mathbf{U} \setminus \mathbf{I} \quad (7)$$

where \mathbf{U} is the universe of possible values for every pixel to take. Then, it is defined the operation for the complement of an image

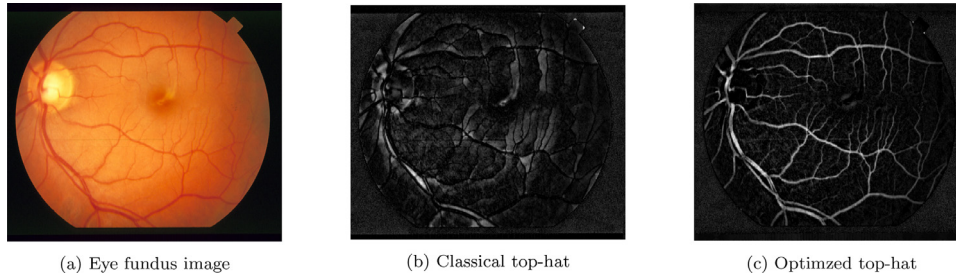


Fig. 3. Most relevant stages of the proposed method

as:

$$I^c(x, y) = \max(U) - I(x, y) \quad (8)$$

For thick vessels enhancement process, the disk-shaped structuring element for both opening (\circ) and closing (\bullet) operations, a radius of eight and sixteen pixels is used, respectively.

Figure 3 c shows the result of the proposed optimized top-hat filter applied on the input fundus image shown in Figure 3 a. Figure 3 b is the result obtained by using the classical top-hat operation expressed in Equation 5. Both images (Figure 3 b and Figure 3 c) are generated by choosing the same shape of the structuring element and size for both opening and closing operation (disk with a radius of twelve pixels). The qualitative analysis of the images show that the proposed optimized top-hat filter enhances the contrast of the vessels much better than the classical top-hat filter, enhancing both thick and thin vessels.

3.2.2. Homomorphic filtering

If it is considered the classical intensity model for digital images, an image can be regarded as the result of the reflected light over a scene, which is then collected by a camera to form the image. Normally this model is denoted in terms of intensity spatial distributions [76] of a two-dimensional function (an image $I(x, y)$ in this case) and is represented as:

$$I(x, y) = I(x, y)r(x, y) \quad (9)$$

where $I(x, y)$ represents the intensity of the illumination and $r(x, y)$ describes the spatial distribution of the reflectance which is generated and dependent on the intrinsic properties of the object and the scene.

The homomorphic filtering is a frequency domain filtering process which allows to adjust illumination and reflectance intensities of an image over a spectral-domain, making possible a diverse analysis by multiple frequency-domain filters [77]. Frequently, the reflectance component $r(x, y)$ is dispersed over the entire frequency domain, while the intensity of illumination component $I(x, y)$ presents smooth variations that are characterized by low spatial frequencies [76,78]. Therefore the illumination component is often located in the center of the 2D-Fourier frequency domain. A common issue in vessel segmentation is the necessity to enhance the reflectance from the fundus image by reducing the contribution of the intensity of the illumination component. In order to solve it, a linear frequency-domain filter is used to diminish the low-frequency and strengthen high-frequency intensities [78].

A mathematical tool that implies the conversion of multiplication to addition is the natural logarithm. Applying this concept to Equation 9 the following equation is obtained:

$$z(x, y) = \ln[I(x, y)] = \ln[I(x, y)r(x, y)] = \ln[I(x, y)] + \ln[r(x, y)] \quad (10)$$

The logarithm is mathematically considered as a homomorphism (hence the filtering process name) that maps from a multiplicative group of numbers to an additive group of numbers, where a

linear filtering process becomes applicable [79]. The Fourier transform is applied to Equation 10, a process that cannot be done directly since the multiplication of two functions is not separable in the Fourier domain.

$$\mathcal{F}\{z(x, y)\} = F_z(u, v) = F_I(u, v) + F_r(u, v) \quad (11)$$

The process of filtering is done by the multiplication of the image $F_z(u, v)$ with a frequency-domain filter $H(u, v)$. From different transfer functions experimentally tested, the Gaussian high-pass response is quite useful for eye fundus images, whose frequency-domain representation is given in Equation 12.

$$H(u, v) = 1 - \exp\left(\frac{-D^2(u, v)}{2\sigma^2}\right) \quad (12)$$

Where $D(u, v) = \sqrt{u^2 + v^2}$ and σ the parameter that measures the dispersion of the Gaussian curve. Larger the value of σ , larger the cut-off frequency and milder the filtering. After applying the filter the following equation is obtained:

$$G(u, v) = F_z(u, v)H(u, v) = F_I(u, v)H(u, v) + F_r(u, v)H(u, v) \quad (13)$$

To recover the filtered spectrum of the processed signal a subsequent inverse Fourier transformation is applied as follows:

$$\mathcal{F}^{-1}\{G(u, v)\} = \mathcal{F}^{-1}\{F_I(u, v)H(u, v)\} + \mathcal{F}^{-1}\{F_r(u, v)H(u, v)\} \quad (14)$$

$$g(x, y) = I'(x, y) + r'(x, y) \quad (15)$$

Finally, the filtered image $I'(x, y)$ is found by an exponential transformation to undo the logarithmic transformation. The final process can be formulated as in Equation 16.

$$I'(x, y) = \exp[g(x, y)] = \exp[I'(x, y)] \exp[r'(x, y)] \quad (16)$$

Illumination and reflectance components are not entirely separated on the spectral-domain, the homomorphic approach is nevertheless a useful tool which image results yields in quite good enhancements [79]. For this case, the σ value is two to enhance thick vessels, whose reflectance value is quite bigger than thin vessels.

3.2.3. Median filter

Before the final operation, a salt and pepper noise generated by a low value of σ in the homomorphic filtering process is removed by a median filter process. The principal feature to highlight is that the median filter preserves edges while removing noise. To some extent, it can distinguish isolated noise from the input image features such as sharp edges, and other image details. This information corresponds to high spatial frequencies i.e. preserving previously enhanced thick vessels. The median filter substitute each pixel in the image with the median of the intensity values within a neighborhood $R(m, n)$. Mathematically, the resultant image $I'(x, y)$ of a median filtering process of an image $I(x, y)$ is formulated as:

$$I'(x, y) = M_e(I(m, n)), (m, n) \in R \quad (17)$$

where M_e is the median value the pixels covered by $R(x, y)$. The noise generated by the previous steps is relatively small but it drastically influences the result. The size of the neighborhood is a $[2, 2]$ matrix.

Lately, the optimized top-hat is used anew to give a better profile of the thick vessels, filling small black pixels regions enclosed in them. In this case, the values of the disk-shaped structuring element are considerably larger compared to the last optimized top-hat process. For both opening and closing operations are proposed with a radius of thirty-two and eighty-six, respectively. The result of the foregoing concepts can be shown in Figure 2 c.

3.3. Segmentation of thin vessels

The thin vessel segmentation process shares two of the detailed stages for thick ones, whose methodology has been previously detailed in Subsection 3.2. Such methods are not detailed in this section. However, the proposed values for those communal stages will be presented in this subsection.

Based on the methodology described in the previous subsection and taking into account that thin blood vessels span a smaller pixel size, the disk-shaped structuring element for both opening and closing operations is proposed with a radius of four and twenty pixels, respectively. The total percentage of the image that thin vessels encompass is too small, therefore percentage of total reflectance component value of them is lower compared to thick vessels. In order to enhance the small white regions a σ value of twenty is used to enlarge the cut-off regions of the filter. Thus generating an improvement in all the white components of the image including the small vessels but causing a thinning in the thick and main veins of the vascular tree, effect that will later be counterbalanced by the splicing of the image generated by the segmentation stages for thick veins over the resultant image of the ensuing steps.

3.3.1. Two-dimensional matched filtering

When a gray-scale image is piecewise analyzed, the contained parts can be similar to a certain distribution curve. The two-dimensional matched filters are designed to enhance image regions that match a specific distribution. Hence, this filtering method searches a certain degree of correlation between the particular distribution and the local image area. The approach of using a matched filtering method is to detect piecewise linear segments of blood vessels in fundus images, whose profile in gray-scale values of the cross-section of the vasculature can be estimated by a Gaussian-shaped curve [80].

This distribution (called kernel) is rotated by an angular step θ and subsequently convolving it with the input image areas in order to intensify the matched regions. The kernel is rotated by using a rotation matrix **RM** expressed as follows:

$$\mathbf{RM} = \begin{bmatrix} \cos \theta & -\sin \theta \\ \sin \theta & \cos \theta \end{bmatrix} \quad (18)$$

Non-vessel regions (i.e. low value of response) are not enhanced. The matched filter kernel is defined as follows:

$$f(x, y) = -k \exp\left(\frac{-x^2}{2\sigma^2}\right), \text{ for } |y| \leq L/2 \quad (19)$$

where L is the length of the piecewise element that the vessel is supposed to have and σ the spread of the kernel intensity profile. Here, it is important to take into account some considerations; in the related literature the blood vessels have low curvatures and it is imperative to look for a rotation of anti-parallel pairs that are estimated piecewise element and also has been noted that small blood vessels have a considerable poor local contrast [81,82]. Although a homomorphic enhancement is previously applied, small

vessels have a low reflectance component when compared against other human eye inner surfaces, its appearance is with a low illumination than the relative background and the width of the vessel diminishes as it travels through the vascular tree. To overcome these considerations the orientation of a vessel may be at any angles and it is taken for granted that the vessel direction is aligned along the y-axis. For thin vessel segmentation the kernel is rotated with an angular step of seven degrees into an angular direction $\theta = 0, 7, 14, \dots, 182$ degrees, giving a total of 26 different rotations. The proposed values for this methodology are a σ value of 0.8, and kernel size of 7×7 pixels, considering that common widths of retinal blood vessels lie within a range of 2 – 10 pixels (36 – 180 μm) [80]. The above method process diminishes the probability of false detection of vasculature, therefore reducing the false positive rate.

3.3.2. MCET-HHO

Finally, the Minimum Cross-Entropy Thresholding - Harris Hawks Optimization (MCET-HHO) [83] method is applied to the image resulting from the coincident filtering, which is a multilevel segmentation algorithm that is used to simplify the intensity levels of the pixels in the image and facilitate the identification of similar regions. This technique consists of minimizing the statistical criterion of cross-entropy as an objective function through the Harris Hawks Optimization (HHO) [84] metaheuristic algorithm to obtain the best threshold values. The Minimum Cross-Entropy Thresholding (MCET) for the multilevel procedure is computed from the Equation 20 to acquire an objective function based on the vector **th**, which contains the different threshold values to segment the image.

$$f_{\text{cross}}(\mathbf{th}) = \sum_{i=1}^L ih(i) \log(i) - \sum_{i=1}^{nt} H_i \quad (20)$$

where nt is the total number of thresholds and H_i is determined as:

$$\begin{aligned} H_1 &= \sum_{i=1}^{th_1-1} ih(i) \log(\mu(1, th_1)) \\ H_k &= \sum_{i=th_{k-1}}^{th_k-1} ih(i) \log(\mu(th_{k-1}, th_k)), \quad 1 < k < nt \\ H_{nt} &= \sum_{i=th_{nt}}^L ih(i) \log(\mu(th_{nt}, L+1)) \end{aligned} \quad (21)$$

The HHO algorithm iterates until the stop criterion is reached evaluating in the cross-entropy function ($f_{\text{cross}}(\mathbf{th})$) until it finds the combination of thresholds that obtain the minimum fitness value.

The HHO parameters used for the optimal segmentation of the thin vessels are 250 iterations as a stop criterion, 30 hawks for the algorithm population, and four optimal thresholds for the vector **th** = $[th_1, th_2, th_3, th_4]$. Once the optimal values have been found to separate the image into different sections using the histogram information, the image is segmented as shown in Equation 22 [85].

$$I_s(x, y) = \begin{cases} th_1, & \text{if } I_{Gr}(x, y) \leq th_1 \\ th_i, & \text{if } th_{i-1} < I_{Gr}(x, y) < th_i, \quad i = 2, 3, \dots, nt - 1 \\ th_{nt}, & \text{if } I_{Gr}(x, y) > th_{nt} \end{cases} \quad (22)$$

where I_s is the segmented image, I_{Gr} is the original image in gray-scale and th_i are the best threshold values (**th**) used to complete the image segmentation. Finally, the image from the four thresholds is binarized for the segmentation of thin vessels as shown in Figure 2 d.

3.4. Post-processing

The merger between thick and thin vessel segmentation in binary format is performed through a bit-wise OR operation, then a

final segmentation image is generated, showing the results of both branches of the flowchart shown in Figure 1.

In order to remove small unwanted elements as well as noise generated by the previous stages, a final post-processing stage is carried out. This stage is composed of morphological image operations such as dilate, erode and a connectivity test where binary elements smaller than the size of a pre-defined pixel are removed, producing a final binary image that can be later evaluated. The final result of the segmentation process is shown in Figure 2 e.

4. Results and Discussion

In this section, the performance results of the proposed method applied over two eye fundus datasets for retinal vessel segmentation is presented: DRIVE [54] and STARE [55], both are publicly available.

The DRIVE dataset consists of 40 images which in turn are sub-grouped into two sets with 20 elements, presented as the training and test sets. All of the eye fundus images were acquired by a Canon CR5 nonmydriatic 3CCD camera with a 45° field of view. The set have a spatial resolution of 565 × 584 pixels [86]. Moreover, the DRIVE image dataset includes manual segmentation manual segmentation performed and approved by three human observers who received training from expert medicals. The training set includes manual segmentation of one set accomplished by one human observer. Differently, the test set was manually segmented by two human observers giving two manual extraction perspectives, thus generating a better analysis criterion, being the latter considered as the ground-truth images used to performance analysis of the methodology detailed in the Section 3.

Otherwise, the STARE dataset is composed of 397 digitalized eye fundus images obtained using a TopCon TVR-50 fundus camera with a 35° field of view and a spatial resolution of 605×700 pixels [55]. Compared to the previously described image dataset, just for 20 of them, manual segmentation was performed by two observers. Where the first one segmented the 10.4% of the whole image pixels as a vascular tree pixel, while the second observer segmented a total of 14.9%. Both datasets include healthy as well as diseased fundus images such as vascular abnormalities, diabetic retinopathy, choroidal neovascularization, arteriosclerotic retinopathy, among many others.

In order to perform an mathematical analysis and obtain a correctness degree of segmentation, three index performance metrics are used: Specificity (*Spe*), Sensitivity (*Sen*) and Accuracy (*Acc*), which are mathematically defined as follows:

$$\text{Specificity}(\text{Spe}) = \frac{T_N}{T_N + F_P} \quad (23)$$

$$\text{Sensitivity}(\text{Sen}) = \frac{T_P}{T_P + F_N} \quad (24)$$

$$\text{Accuracy}(\text{Acc}) = \frac{T_P + T_N}{T_P + T_N + F_P + F_N} \quad (25)$$

where T_P (True positive) represents the pixel amount considered as a vessel in the ground-truth and the segmented image. T_N (True Negative) refers to the pixel number correctly classified as non-vessel in ground-truth and segmented image. Meanwhile, F_P (False Positive) represents the pixel amount considered as a vessel in the segmented image, but non-vessel pixels the ground-truth. By last, F_N (False Negative) shows the pixel number incorrectly classified as non-vessel in the segmented image when they match to a vessel in the ground-truth.

In Table 1, the performance results are presented by applying the previously detailed segmentation metrics obtained by the proposed methodology against observer 1 and observer 2 for the

Table 1
Results of the proposed methodology applied to DRIVE dataset

Images	DRIVE observer 1			DRIVE observer 2		
	Spe	Sen	Acc	Spe	Sen	Acc
01_test	0.9783	0.8159	0.9644	0.9787	0.8295	0.9656
02_test	0.9859	0.7850	0.9654	0.9877	0.8132	0.9701
03_test	0.9775	0.7433	0.9542	0.9751	0.8051	0.9600
04_test	0.9917	0.6974	0.9646	0.9912	0.7267	0.9680
05_test	0.9929	0.6187	0.9578	0.9930	0.7138	0.9703
06_test	0.9858	0.6807	0.9561	0.9873	0.7254	0.9629
07_test	0.9879	0.6998	0.9616	0.9820	0.8127	0.9699
08_test	0.9924	0.6072	0.9593	0.9877	0.7153	0.9695
09_test	0.9875	0.7006	0.9642	0.9887	0.7165	0.9667
10_test	0.9858	0.7392	0.9650	0.9829	0.8157	0.9709
11_test	0.9893	0.6880	0.9623	0.9900	0.7473	0.9698
12_test	0.9878	0.6953	0.9625	0.9876	0.7443	0.9681
13_test	0.9883	0.6989	0.9600	0.9907	0.6966	0.9609
14_test	0.9799	0.7791	0.9637	0.9787	0.8272	0.9674
15_test	0.9874	0.6829	0.9656	0.9852	0.6280	0.9586
16_test	0.9893	0.7349	0.9663	0.9895	0.7811	0.9717
17_test	0.9826	0.7340	0.9616	0.9806	0.8103	0.9680
18_test	0.9814	0.7799	0.9654	0.9893	0.7535	0.9677
19_test	0.9839	0.8479	0.9726	0.9884	0.7523	0.9650
20_test	0.9763	0.8241	0.9651	0.9847	0.7416	0.9622
Mean	0.9856	0.7276	0.9629	0.9860	0.7578	0.9667

Table 2
Results of the proposed methodology applied to STARE dataset

Images	STARE observer 1			STARE observer 2		
	Spe	Sen	Acc	Spe	Sen	Acc
im0001	0.9635	0.7155	0.9414	0.9610	0.6473	0.9342
im0002	0.9618	0.5965	0.9421	0.9668	0.6246	0.9431
im0003	0.9476	0.8606	0.9514	0.9572	0.7364	0.9355
im0004	0.9622	0.5745	0.9414	0.9707	0.5798	0.9274
im0005	0.9794	0.7354	0.9566	0.9785	0.6432	0.9441
im0044	0.9897	0.4432	0.9448	0.9824	0.4335	0.9147
im0077	0.9928	0.8423	0.9666	0.9775	0.6311	0.9458
im0081	0.9924	0.9090	0.9694	0.9743	0.6194	0.9412
im0082	0.9921	0.8306	0.9689	0.9807	0.6217	0.9467
im0139	0.9956	0.7877	0.9667	0.9823	0.5967	0.9194
im0162	0.9927	0.8101	0.9682	0.9803	0.6047	0.9482
im0163	0.9898	0.8836	0.9655	0.9724	0.7316	0.9599
im0235	0.9937	0.8350	0.9629	0.9754	0.6472	0.9448
im0236	0.9924	0.8300	0.9652	0.9787	0.6628	0.9486
im0239	0.9847	0.8412	0.9552	0.9660	0.7207	0.9516
im0240	0.9912	0.6339	0.9429	0.9781	0.5045	0.9186
im0255	0.9964	0.7215	0.9637	0.9875	0.5555	0.9386
im0291	0.9953	0.6612	0.9760	0.9927	0.5825	0.9722
im0319	0.9876	0.7612	0.9715	0.9807	0.6319	0.9653
im0324	0.9703	0.6755	0.9390	0.9579	0.5787	0.9313
Mean	0.9836	0.7474	0.9580	0.9751	0.6177	0.9414

DRIVE dataset. The specificity, sensitivity and average precision of the method against observer 1 are 0.9856, 0.7276 and 0.9629, respectively. Likewise, the averages of the metrics against observer 2 are 0.9860, 0.7578 and 0.9667. The maximum specificity values against observers 1 and 2 are 0.9929 and 0.9930 in image 05_test. While the minimum values against observers 1 and 2 are 0.9763 and 0.9751 in images 20_test and 03_test, respectively.

In Table 2, the results of the metrics when comparing the segmentation performed by the proposed method with both observers for the STARE data-set are presented. The average of the specificity, sensitivity and accuracy obtained when the segmented image is compared to the ground-truth of observer 1 is 0.9836, 0.7474 and, 0.9580, and when comparing with the ground-truth observer 2, they are 0.9751, 0.6177 and, 0.9414. The maximum values of the specificity metric against observers 1 and 2 are 0.9414 in image im0255 and 0.9927 in image im0291, respectively. While the min-

Table 3

Results comparison between the proposed methodology applied to both DRIVE and STARE dataset and supervised and unsupervised state-of-the-art methods

Methods	Year	DRIVE dataset			STARE dataset			Processing
		Spe	Sen	Acc	Spe	Sen	Acc	time
Supervised methods								
Liskowski et al. [53]	2016	0.9241	0.9230	0.9160	0.9304	0.9207	0.9309	92.0s
Zhang et al. [87]	2017	0.9712	0.7861	0.9466	0.9729	0.7882	0.9547	23.40s*
Orlando et al. [2]	2017	0.9684	0.7897	-	0.9738	0.7680	-	-
Dasgupta et al. [88]	2017	0.9801	0.7691	0.9533	-	-	-	-
Yan et al. [89]	2018	0.9818	0.7653	0.9542	0.9846	0.7581	0.9612	-
Thangaraj et al. [90]	2018	0.9753	0.8014	0.9606	0.9536	0.8339	0.9435	180.86s
Guo et al. [91]	2018	0.9806	0.7046	0.9613	0.9816	0.5629	0.9540	-
Yang et al. [65]	2019	0.9696	0.7560	0.9421	0.9733	0.7202	0.9477	-
Jin et al. [66]	2019	0.9800	0.7963	0.9566	0.9878	0.7595	0.9641	17.65s
Cheng et al. [67]	2020	0.9834	0.7672	0.9559	-	-	-	-
Adapa et al. [64]	2020	0.9811	0.6994	0.9450	0.9839	0.6298	0.9486	81.0s
Wu et al. [68]	2020	0.9813	0.7996	0.9582	0.9863	0.7963	0.9672	88.0s
Unsupervised methods								
Zhang et al. [92]	2016	0.9725	0.7743	0.9476	0.9758	0.7791	0.9554	20.0s
Shahid et al. [93]	2017	0.9790	0.7300	0.9580	0.9650	0.7900	0.9510	-
Fan et al. [94]	2018	0.9810	0.7360	0.9610	0.9710	0.7910	0.9570	13.23s
Aguirre et al. [95]	2018	-	0.7854	0.9503	0.9454	0.7116	0.9231	-
Abdallah et al. [96]	2018	0.9765	0.6887	0.9389	0.9711	0.6801	0.9388	-
Pal et al. [97]	2018	0.9744	0.6129	0.9431	-	-	-	-
Yue et al. [98]	2018	0.9731	0.7528	0.9447	-	-	-	4.60s*
Biswal et al. [99]	2018	0.9700	0.7100	0.9500	0.9700	0.7000	0.9500	3.30s
Diaz et al. [59]	2019	0.9701	0.8464	0.9619	0.9619	0.8331	0.9559	-
Wang et al. [58]	2019	0.9775	0.7287	0.9446	0.9733	0.7526	0.9503	4.50s
Roy et al. [100]	2019	0.9622	0.4392	0.9295	0.9718	0.4317	0.9488	0.10s
Zhou et al. [62]	2020	0.9803	0.7262	0.9475	0.9730	0.7865	0.9535	63.2s
Dos Santos et al. [61]	2020	0.9695	0.7702	0.9519	-	-	-	-
Shukla et al. [60]	2020	0.9836	0.7015	0.9476	0.9863	0.7023	0.9573	1.41s
Pachade et al. [63]	2020	0.9721	0.7738	0.9552	0.9688	0.7769	0.9543	4.78s
Proposed		0.9860	0.7578	0.9667	0.9836	0.7474	0.9580	1.74s

imum values against observers 1 and 2 are 0.9476 and 0.9572 in the image *im0003*.

To perform a numerical contrast of the obtained results against the supervised and unsupervised up-to-date methods, in Table 3, the efficiency and computing time results for both datasets are presented. As shown in this table, the average highest values in the three metrics for supervised and unsupervised methods are in bold type. The highest values comparing both methods, supervised and unsupervised, in specificity and accuracy are achieved by this methodology with 0.9860 and 0.9667, while sensitivity by Liskowski et al. [53] with 0.9230 for DRIVE dataset. Furthermore, for STARE dataset, the highest values in specificity are obtained by Jin et al. [66] with 0.9878, while the sensitivity by Liskowski et al. [53] with a value of 0.9207 and finally, Wu et al. [68] present the highest value of accuracy with 0.9672. In this last dataset, the proposed method presents a specificity of 0.9836 and an accuracy of 0.9580. Although this does not present the best results, it is important to highlight that it is numerically very close to the methods that require a training process and a ground-truth, such as supervised methods, which are also computationally more expensive.

The average processing times calculated for each method shown in Table 3 were obtained from the literature. The values with asterisk (*) represent the processing time calculated only for the images from DRIVE database. From Table 3, it is evident the proposed approach offers a reduced processing time relative to the supervised methods and unsupervised methods. The proposed algorithm presents competitive processing time values among the supervised methods and unsupervised methods; even though the MCET-HHO algorithm is iterative and evaluates 30 hawks, the calculation time is not too long since the problem is only 4-dimensional. Additionally, the proposed approach provides the best efficiency values when calculating the three-performance metrics.

It is important to notice that the vascular tree decreases their width as the length is advanced, therefore the size of the vessels is smaller at the ends of the branches compared to branches near the beginning of the tree. In Figure 4, it is presented a comparative for small vessel segmentation between this method, DRIVE and STARE observers, and eye fundus image. The original images of DRIVE and STARE are shown in Figure 4 a and Figure 4 e, respectively. A crop is made in a 200×200 pixel region in order to make the differences more noticeable, which is framed in a red square for both the human observer segmentation and the final segmentation images.

For DRIVE images, the manual segmentation between observer 1 and observer 2 (Figure 4 b and Figure 4 c, respectively) shows similarities in the minimum thickness of the segmented vessel, however, each one performed a different segmentation. The observer 2 in DRIVE dataset made a meticulous small vessel segmentation near to the macula zone than observer 1, while the proposed method (Figure 4 d) clearly has a better performance than observer 1, but quite lower than observer 2. The total of smallest central ramifications are started by the proposed method but not quite finished with the corresponding length, however, small variations in non-vessel regions due to small intensity fluctuations are not generated, thus maintaining the purpose of having a low rate of false positives. In comparison with the smallest vessel segmentation made by human observers, the proposed methodology presents very good results.

Moreover, there is a very large difference in thin vessel manual segmentation between observer 1 (Figure 4 f) and observer 2 (Figure 4 g) for STARE dataset. The vessel thickness segmentation of observer 2 is way smaller than observer 1, hence the sensibility differences between STARE observers shown in Table 2. However, the visual comparison between manual and proposed method seg-

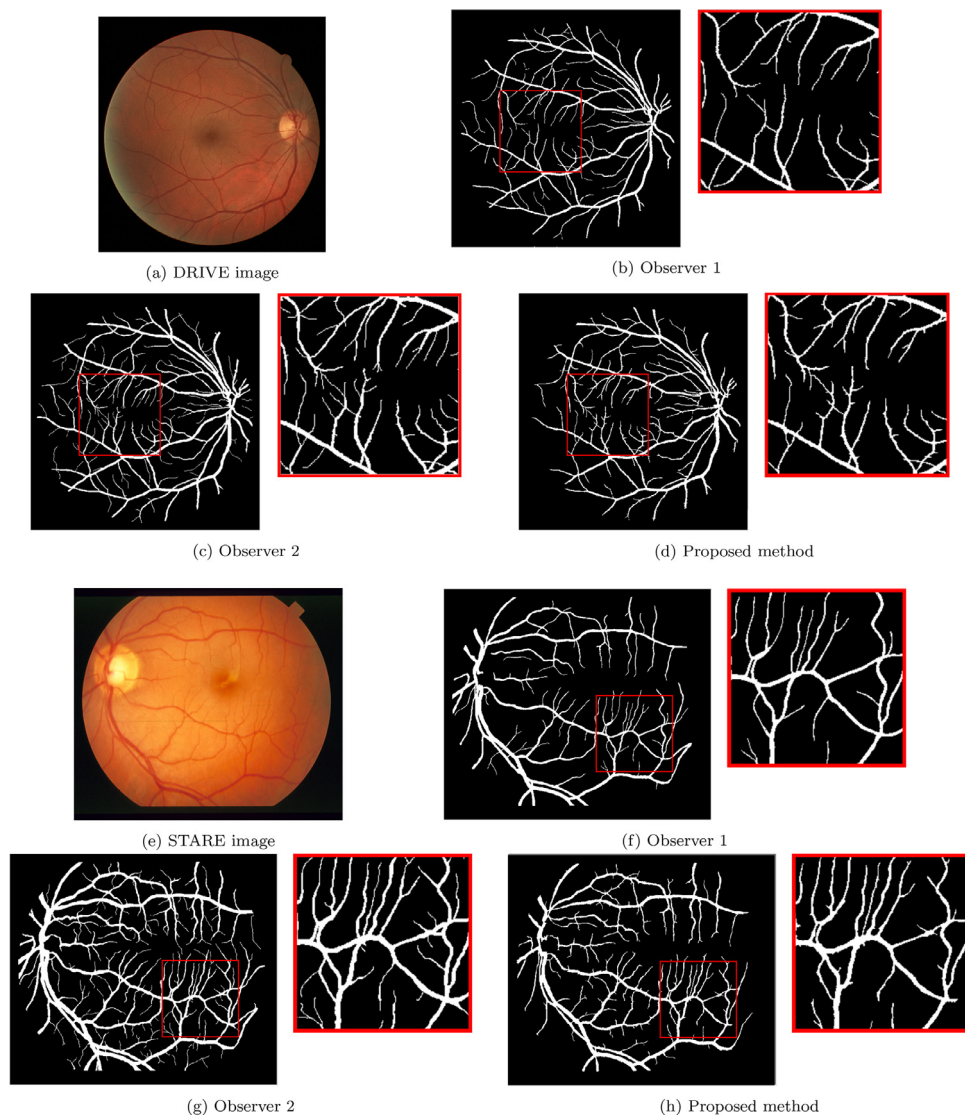


Fig. 4. Thin vessels segmentation comparison between manual segmentation of DRIVE and STARE dataset (19_test and im0236 images respectively) and the proposed method

mentation images shows that there are just a few differences in the small vessel detection, thus reaffirming the practical functionality of the method.

In [Figure 5](#) and [Figure 6](#) the variability between the obtained segmentation and the corresponding observers from DRIVE and STARE dataset, respectively, is graphically shown. In [Figure 5 a](#) and [Figure 6 a](#) the original image is shown and [Figure 5 b](#) and [Figure 6 b](#) shows the red-colored proposed method segmentation region juxtaposed with green channel background. [Figure 5 c](#) and [6 c](#) shows the green-colored manual segmentation made by the observer 1 on DRIVE and STARE dataset, respectively, while analogously [Figure 5 d](#) and [6 d](#) shows the manual segmentation made by the observer 2, the four images also juxtaposed with green channel background.

Following this color scheme, [Figure 5 e](#) shows the variation obtained from the method with respect to the segmentation manually performed where the yellow color corresponds to the matching in segmentation with the observer 1, while [Figure 5 f](#) shows the segmentation comparison with observer 2. Similarly, [Figure 6 e](#) and [Figure 6 f](#) shows the graphical comparison with the observer 1 and observer 2 of STARE dataset, respectively. The results of the variability show that in the case of STARE compared to observer

1, much better segmentation is obtained and can be seen where the red color of the segmentation predominates, whereas with respect to the observer 2, a few small vessels have not been segmented, mostly away from the center of the image. The proposed approach has certain shortcomings by segmenting vascular arcades near the outside ring of the eye fundus image that can be seen in the demonstrated results. However, the damage of blood vessels that represent useful information about direct harm to central vision is found near the center of the eye fundus image, i.e. the macular zone, where the results are significantly good. The above is shown in [Figure 4](#).

This method presents good results when applied to pathological images. In some cases, disease signs such as microaneurysms, exudates, drusens or hemorrhages show a notorious contrast in the fundus image and are visually noticeable. In [Figure 7](#), DRIVE 14_test image and its segmentation result are shown. The authors of the dataset tagged this as a diabetic retinopathy case. In [Figure 7 a](#), two of several abnormalities that appear in the image are marked in a green and blue square of 50×50 pixels over the original image and are up-sized for a better observation. As can be seen in [Figure 7 b](#), the segmentation result does not include any abnormalities appearing in the original fundus image. Thus giving

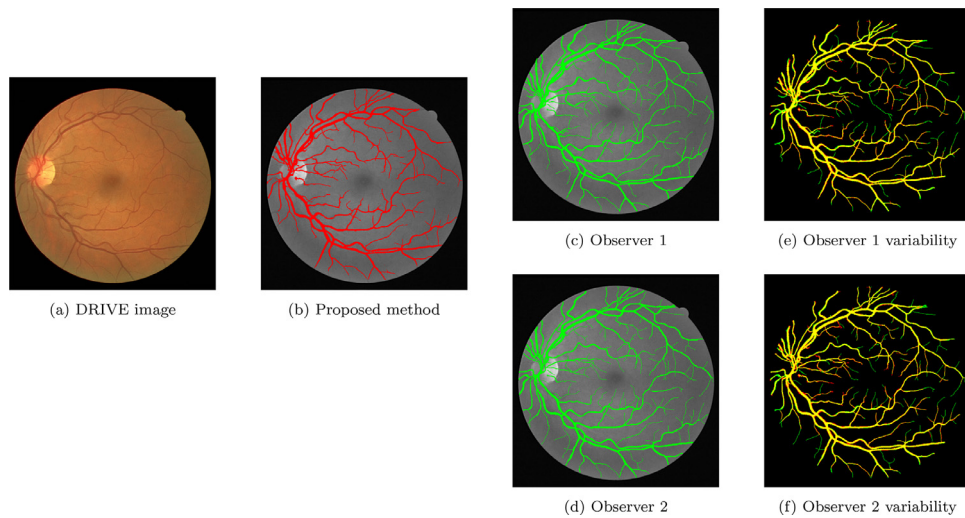


Fig. 5. Segmentation result comparison of DRIVE 01_test image between human observers and the proposed approach

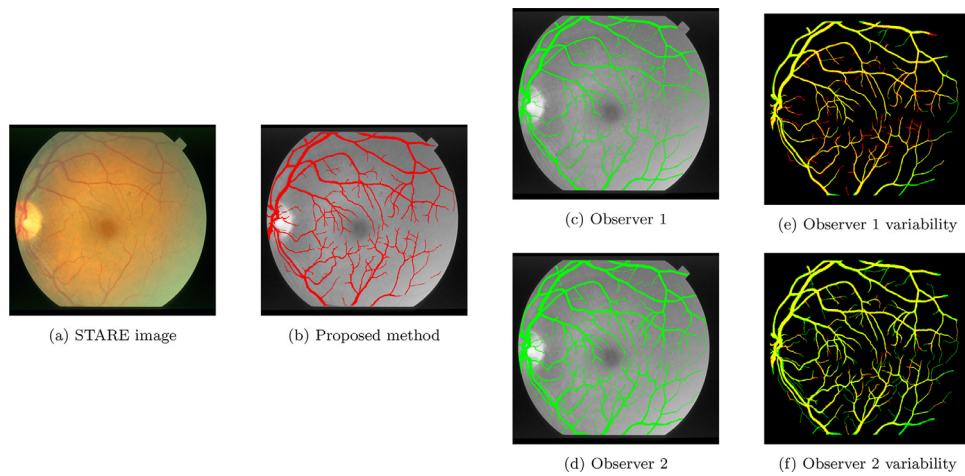


Fig. 6. Segmentation result comparison of STARE im0239 image between human observers and the proposed approach

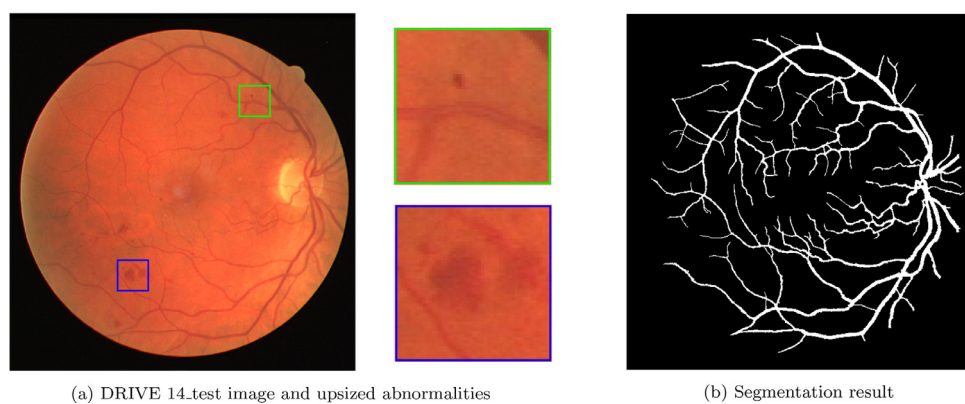


Fig. 7. Fundus image of a diabetic retinopathy case and its segmentation

a visual corroboration of the high specificity value obtained by this proposal.

5. Conclusions and Further work

A novel methodology depicting an improvement in the retinal vascular tree segmentation on the human eye fundus image is pre-

sented, whose basic foundation is the segmentation process in two branches: thin and thick vessel detection. The proposed method demonstrates high-specificity performance without the need for manual segmentation for learning or training techniques that require superior performance but at a high computational cost. The results obtained when comparing the segmentation result of the proposed approach applied to both DRIVE and STARE dataset, show

that this method surpasses all the unsupervised methods compared to those found in the literature. Furthermore, it is relevant to remark that more precise visual results are recorded in the extraction of the thin vessels compared to the reviewed methods of the literature.

The essence of the presented framework lies in the parameter variation of the optimized top-hat and homomorphic filtering stages, which depends on the result of the segmentation, thin and thick vessels in this case. This feature is essential to obtain better accuracy and specificity in the segmentation process. One of the main disadvantages of the proposal is that a low sensitivity value is obtained compared to the values specified in the state-of-the-art. Also, for the parameter settings of the optimized top-hat and the homomorphic filtering, a run of various experiments is performed. Therefore, as forthcoming work, it is planned to apply reinforced learning algorithms to balance and obtain the optimal parameters of the proposed methodology to increase the average of the sensitivity metric.

Finally, it is intended to use this method as a pre-processing stage in a robust CADx system in healthy and unhealthy eye fundus for disease classification by segmenting the retinal vessels. To achieve this, the key is a high specificity segmentation value, i.e. a low value of false positive (which may represent an erroneous interpretation at the diagnostic stage), the latter being the approach that was taken into account in the development of this proposal.

Declaration of Competing Interest

The authors declare that they have no known competing financial interests or personal relationships that could have appeared to influence the work reported in this paper.

References

- [1] I.P. Chatziralli, E.D. Kanonidou, P. Keryttopoulos, P. Dimitriadis, L.E. Papazisis, The value of funduscopy in general practice, *The open ophthalmology journal* 6 (2012) 4.
- [2] J.I. Orlando, E. Prokofyeva, M.B. Blaschko, A discriminatively trained fully connected conditional random field model for blood vessel segmentation in fundus images, *IEEE transactions on Biomedical Engineering* 64 (1) (2016) 16–27.
- [3] J.J. Kanski, B. Bowling, *Clinical ophthalmology: a systematic approach*, Elsevier Health Sciences, 2011.
- [4] Y.Q. Zhao, X.H. Wang, X.F. Wang, F.Y. Shih, Retinal vessels segmentation based on level set and region growing, *Pattern Recognition* 47 (7) (2014) 2437–2446.
- [5] X. Xiao, S. Lian, Z. Luo, S. Li, Weighted res-unet for high-quality retina vessel segmentation, in: 2018 9th International Conference on Information Technology in Medicine and Education (ITME), IEEE, 2018, pp. 327–331.
- [6] M. Ortega, M.G. Penedo, J. Rouco, N. Barreira, M.J. Carreira, Personal verification based on extraction and characterisation of retinal feature points, *Journal of Visual Languages & Computing* 20 (2) (2009) 80–90.
- [7] R. Vega, G. Sanchez-Ante, L.E. Falcon-Morales, H. Sossa, E. Guevara, Retinal vessel extraction using lattice neural networks with dendritic processing, *Computers in biology and medicine* 58 (2015) 20–30.
- [8] Y. Gavet, M. Fernandes, J. Debayle, J.-C. Pinoli, Dissimilarity criteria and their comparison for quantitative evaluation of image segmentation: application to human retina vessels, *Machine vision and applications* 25 (8) (2014) 1953–1966.
- [9] B. Yin, H. Li, B. Sheng, X. Hou, Y. Chen, W. Wu, P. Li, R. Shen, Y. Bao, W. Jia, Vessel extraction from non-fluorescein fundus images using orientation-aware detector, *Medical image analysis* 26 (1) (2015) 232–242.
- [10] L.C. Neto, G.L. Ramalho, J.F.R. Neto, R.M. Veras, F.N. Medeiros, An unsupervised coarse-to-fine algorithm for blood vessel segmentation in fundus images, *Expert Systems with Applications* 78 (2017) 182–192.
- [11] Q. Li, B. Feng, L. Xie, P. Liang, H. Zhang, T. Wang, A cross-modality learning approach for vessel segmentation in retinal images, *IEEE transactions on medical imaging* 35 (1) (2015) 109–118.
- [12] Y. Zhao, J. Xie, H. Zhang, Y. Zheng, Y. Zhao, H. Qi, Y. Zhao, P. Su, J. Liu, Y. Liu, Retinal vascular network topology reconstruction and artery/vein classification via dominant set clustering, *IEEE transactions on medical imaging* (2019).
- [13] J. Mo, L. Zhang, Multi-level deep supervised networks for retinal vessel segmentation, *International journal of computer assisted radiology and surgery* 12 (12) (2017) 2181–2193.
- [14] L. Mou, L. Chen, J. Cheng, Z. Gu, Y. Zhao, J. Liu, Dense dilated network with probability regularized walk for vessel detection, *IEEE transactions on medical imaging* (2019).
- [15] M.M. Fraz, P. Remagnino, A. Hoppe, B. Uyyanonvara, A.R. Rudnicka, C.G. Owen, S.A. Barman, Blood vessel segmentation methodologies in retinal images—a survey, *Computer methods and programs in biomedicine* 108 (1) (2012) 407–433.
- [16] J.M. Patel, N.C. Gamit, A review on feature extraction techniques in content based image retrieval, in: 2016 International Conference on Wireless Communications, Signal Processing and Networking (WiSPNET), IEEE, 2016, pp. 2259–2263.
- [17] R. Vaddi, M. Prabukumar, Comparative study of feature extraction techniques for hyper spectral remote sensing image classification: a survey, in: 2017 International Conference on Intelligent Computing and Control Systems (ICICCS), IEEE, 2017, pp. 543–548.
- [18] B.S. Vidya, E. Chandra, Entropy based local binary pattern (elbp) feature extraction technique of multimodal biometrics as defence mechanism for cloud storage, *Alexandria Engineering Journal* 58 (1) (2019) 103–114.
- [19] R.A. Ibrahim, A.A. Ewees, D. Oliva, M. Abd Elaziz, S. Lu, Improved salp swarm algorithm based on particle swarm optimization for feature selection, *Journal of Ambient Intelligence and Humanized Computing* 10 (8) (2019) 3155–3169.
- [20] A.A. Ewees, M. Abd El Aziz, A.E. Hassanien, Chaotic multi-verse optimizer-based feature selection, *Neural computing and applications* 31 (4) (2019) 991–1006.
- [21] Y. Zhang, R. Liu, X. Wang, H. Chen, C. Li, Boosted binary harris hawks optimizer and feature selection, *structure* 25 (2020) 26.
- [22] D. Liu, S. Wang, D. Huang, G. Deng, F. Zeng, H. Chen, Medical image classification using spatial adjacent histogram based on adaptive local binary patterns, *Computers in biology and medicine* 72 (2016) 185–200.
- [23] H. Chantar, M. Mafarja, H. Alsawalqah, A.A. Heidari, I. Aljarah, H. Faris, Feature selection using binary grey wolf optimizer with elite-based crossover for arabic text classification, *Neural Computing and Applications* 32 (16) (2020) 12201–12220.
- [24] H. Tang, Y. Xu, A. Lin, A.A. Heidari, M. Wang, H. Chen, Y. Luo, C. Li, Predicting green consumption behaviors of students using efficient firefly grey wolf-assisted k-nearest neighbor classifiers, *IEEE Access* 8 (2020) 35546–35562.
- [25] M. Ahmad, S. Shabbir, D. Oliva, M. Mazzara, S. Distefano, Spatial-prior generalized fuzziness extreme learning machine autoencoder-based active learning for hyperspectral image classification, *Optik* 206 (2020) 163712.
- [26] J. Sivic, A. Zisserman, Video google: A text retrieval approach to object matching in videos, in: null, IEEE, 2003, p. 1470.
- [27] V. Nguyen, M. Blumenstein, An application of the 2d gaussian filter for enhancing feature extraction in off-line signature verification, in: 2011 International Conference on Document Analysis and Recognition, IEEE, 2011, pp. 339–343.
- [28] Y. Hamamoto, S. Uchimura, M. Watanabe, T. Yasuda, Y. Mitani, S. Tomita, A gabor filter-based method for recognizing handwritten numerals, *Pattern recognition* 31 (4) (1998) 395–400.
- [29] D.J. Reddy, T.A. Prasath, M.P. Rajasekaran, G. Vishnuvarthanan, Brain and pancreatic tumor classification based on glcm??k-nn approaches, in: International Conference on Intelligent Computing and Applications, Springer, 2019, pp. 293–302.
- [30] A. Subudhi, M. Dash, S. Sabut, Automated segmentation and classification of brain stroke using expectation-maximization and random forest classifier, *Biocybernetics and Biomedical Engineering* 40 (1) (2020) 277–289.
- [31] E. Rodríguez-Esparza, L.A. Zanella-Calzada, D. Oliva, M. Pérez-Cisneros, Automatic detection and classification of abnormal tissues on digital mammograms based on a bag-of-visual-words approach, in: *Medical Imaging 2020: Computer-Aided Diagnosis*, 11314, International Society for Optics and Photonics, 2020, p. 1131424.
- [32] B.A. Devi, M.P. Rajasekaran, Performance evaluation of mri pancreas image classification using artificial neural network (ann), in: *Smart Intelligent Computing and Applications*, Springer, 2019, pp. 671–681.
- [33] L. Nanni, S. Ghidoni, S. Brahnam, Handcrafted vs. non-handcrafted features for computer vision classification, *Pattern Recognition* 71 (2017) 158–172.
- [34] Y. Zaychenko, G. Hamidov, Hybrid fuzzy cnn network in the problem of medical images classification and diagnostics, in: *The International Conference on Natural Computation, Fuzzy Systems and Knowledge Discovery*, Springer, 2019, pp. 883–891.
- [35] S.A. Kumar, J.S. Kumar, A review on recent developments for the retinal vessel segmentation methodologies and exudate detection in fundus images using deep learning algorithms, in: *International Conference On Computational Vision and Bio Inspired Computing*, Springer, 2019, pp. 1363–1370.
- [36] P. Xiuqin, Q. Zhang, H. Zhang, S. Li, A fundus retinal vessels segmentation scheme based on the improved deep learning u-net model, *IEEE Access* 7 (2019) 122634–122643.
- [37] V. Aggarwal, A. Gupta, Integrating morphological edge detection and mutual information for nonrigid registration of medical images, *Current Medical Imaging Reviews* 15 (3) (2019) 292–300.
- [38] M. Raman, R. Korah, K. Tamilselvan, An automatic localization of optic disc in low resolution retinal images by modified directional matched filter, *Int. Arab. J. Inf. Technol.* 16 (1) (2019) 1–7.
- [39] J. Liu, J. Li, K. Zhang, U.A. Bhatti, Y. Ai, Zero-watermarking algorithm for medical images based on dual-tree complex wavelet transform and discrete cosine transform, *Journal of Medical Imaging and Health Informatics* 9 (1) (2019) 188–194.
- [40] L. Satapathy, R. Tripathy, P. Das, A combination of variational mode decomposition and histogram equalization for image enhancement, *National Academy Science Letters* 42 (4) (2019) 333–336.

- [41] T. Jerman, F. Pernuš, B. Likar, Ž. Špiclin, Enhancement of vascular structures in 3d and 2d angiographic images, *IEEE transactions on medical imaging* 35 (9) (2016) 2107–2118.
- [42] R.K. Meleppat, E.B. Miller, S.K. Manna, P. Zhang, E.N. Pugh Jr, R.J. Zawadzki, Multiscale hessian filtering for enhancement of oct angiography images, in: *Ophthalmic Technologies XXIX*, 10858, International Society for Optics and Photonics, 2019, p. 108581K.
- [43] F. Shaik, J. Chittamma, S.M. Islam, B.L. Reddy, S.D. Reddy, Enhancement of cerebral and retinal vascular structures using hessian based filters, in: *ICCC 2020*, Springer, 2020, pp. 461–474.
- [44] S. Hinojosa, K.G. Dhal, M.A. Elaziz, D. Oliva, E. Cuevas, Entropy-based imagery segmentation for breast histology using the stochastic fractal search, *Neurocomputing* 321 (2018) 201–215.
- [45] H. Andrea, I. Aranguren, D. Oliva, M. Abd Elaziz, E. Cuevas, Efficient image segmentation through 2d histograms and an improved owl search algorithm, *International Journal of Machine Learning and Cybernetics* (2020) 1–20.
- [46] G.R. Hernández, M.A. Navarro, N. Ortega-Sánchez, D. Oliva, M. Pérez-Cisneros, Failure detection on electronic systems using thermal images and metaheuristic algorithms, *IEEE Latin America Transactions* 18 (08) (2020) 1371–1380.
- [47] M. Abd Elaziz, A.A. Ewees, D. Oliva, Hyper-heuristic method for multilevel thresholding image segmentation, *Expert Systems with Applications* 146 (2020) 113201.
- [48] I. Aranguren, A. Valdivia, B. Morales-Castañeda, D. Oliva, M. Abd Elaziz, M. Perez-Cisneros, Improving the segmentation of magnetic resonance brain images using the Ishade optimization algorithm, *Biomedical Signal Processing and Control* 64 (2021) 102259.
- [49] T.M. Khan, M. Mehmood, S.S. Naqvi, M.F.U. Butt, A region growing and local adaptive thresholding-based optic disc detection, *Plos one* 15 (1) (2020) e0227566.
- [50] S. Chakraborty, S. Chatterjee, A. Das, K. Mali, Penalized fuzzy c-means enabled hybrid region growing in segmenting medical images, in: *Hybrid Machine Intelligence for Medical Image Analysis*, Springer, 2020, pp. 41–65.
- [51] A. Rampun, B.W. Scotney, P.J. Morrow, H. Wang, J. Winder, Segmentation of breast mr images using a generalised 2d mathematical model with inflation and deflation forces of active contours, *Artificial intelligence in medicine* 97 (2019) 44–60.
- [52] E.R. Arce-Santana, A.R. Mejia-Rodríguez, E. Martinez-Peña, A. Alba, M. Mendez, E. Scalco, A. Mastropietro, G. Rizzo, A new probabilistic active contour region-based method for multiclass medical image segmentation, *Medical & biological engineering & computing* 57 (3) (2019) 565–576.
- [53] P. Liskowski, K. Krawiec, Segmenting retinal blood vessels with deep neural networks, *IEEE transactions on medical imaging* 35 (11) (2016) 2369–2380.
- [54] J. Staal, M.D. Abramoff, M. Niemeijer, M.A. Viergever, B. Van Ginneken, Ridge-based vessel segmentation in color images of the retina, *IEEE transactions on medical imaging* 23 (4) (2004) 501–509.
- [55] A. Hoover, V. Kouznetsova, M. Goldbaum, Locating blood vessels in retinal images by piecewise threshold probing of a matched filter response, *IEEE Transactions on Medical imaging* 19 (3) (2000) 203–210.
- [56] E. Rodríguez-Esparza, L.A. Zanella-Calzada, D. Oliva, S. Hinojosa, M. Pérez-Cisneros, Multilevel segmentation for automatic detection of malignant masses in digital mammograms based on threshold comparison, in: *2019 IEEE Latin American Conference on Computational Intelligence (LA-CCI)*, IEEE, 2019, pp. 1–6.
- [57] E. Rodríguez-Esparza, L.A. Zanella-Calzada, D. Zaldivar, C.E. Galván-Tejada, Automatic detection of malignant masses in digital mammograms based on a mset-hho approach, in: *Applications of Hybrid Metaheuristic Algorithms for Image Processing*, Springer, 2020, pp. 351–374.
- [58] W. Wang, W. Wang, Z. Hu, Segmenting retinal vessels with revised top-bottom-hat transformation and flattening of minimum circumscribed ellipse, *Medical & biological engineering & computing* 57 (7) (2019) 1481–1496.
- [59] D. Primitivo, R. Alma, C. Erik, V. Arturo, C. Edgar, P.-C. Marco, Z. Daniel, A hybrid method for blood vessel segmentation in images, *Biocybernetics and Biomedical Engineering* 39 (3) (2019) 814–824.
- [60] A.K. Shukla, R.K. Pandey, R.B. Pachori, A fractional filter based efficient algorithm for retinal blood vessel segmentation, *Biomedical Signal Processing and Control* 59 (2020) 101883.
- [61] J.C.M. dos Santos, G.A. Carrijo, C.d.F. dos Santos Cardoso, J.C. Ferreira, P.M. Sousa, A.C. Patrocinio, Fundus image quality enhancement for blood vessel detection via a neural network using clahe and wiener filter, *Research on Biomedical Engineering* (2020) 1–13.
- [62] C. Zhou, X. Zhang, H. Chen, A new robust method for blood vessel segmentation in retinal fundus images based on weighted line detector and hidden markov model, *Computer Methods and Programs in Biomedicine* 187 (2020) 105231.
- [63] S. Pachade, P. Porwal, M. Kokare, L. Giancardo, F. Meriaudeau, Retinal vasculature segmentation and measurement framework for color fundus and slo images, *Biocybernetics and Biomedical Engineering* (2020).
- [64] D. Adapa, A.N. Joseph Raj, S.N. Alisetti, Z. Zhuang, G. Naik, A supervised blood vessel segmentation technique for digital fundus images using zernike moment based features, *Plos one* 15 (3) (2020) e0229831.
- [65] Y. Yang, F. Shao, Z. Fu, R. Fu, Discriminative dictionary learning for retinal vessel segmentation using fusion of multiple features, *Signal, Image and Video Processing* 13 (8) (2019) 1529–1537.
- [66] Q. Jin, Z. Meng, T.D. Pham, Q. Chen, L. Wei, R. Su, Dunet: A deformable network for retinal vessel segmentation, *Knowledge-Based Systems* 178 (2019) 149–162.
- [67] Y. Cheng, M. Ma, L. Zhang, C. Jin, L. Ma, Y. Zhou, Retinal blood vessel segmentation based on densely connected u-net, *Mathematical Biosciences and Engineering* 17 (4) (2020) 3088.
- [68] Y. Wu, Y. Xia, Y. Song, Y. Zhang, W. Cai, Nfn+: A novel network followed network for retinal vessel segmentation, *Neural Networks* (2020).
- [69] J.V. Soares, J.J. Leandro, R.M. Cesar, H.F. Jelinek, M.J. Cree, Retinal vessel segmentation using the 2-d gabor wavelet and supervised classification, *IEEE Transactions on medical imaging* 25 (9) (2006) 1214–1222.
- [70] M.S. Livingstone, D.H. Hubel, Psychophysical evidence for separate channels for the perception of form, color, movement, and depth, *Journal of Neuroscience* 7 (11) (1987) 3416–3468.
- [71] R.C. Gonzalez, R. Woods, *Digital Image Processing*, Prentice Hall, 2002.
- [72] E.R. Dougherty, *Mathematical morphology in image processing*, Marcel Dekker, 1992.
- [73] P. Salembier, Comparison of some morphological segmentation algorithms based on contrast enhancement. application to automatic defect detection., in: *5. European Signal Processing Conference.*, 2, 1990, pp. 833–836.
- [74] A.M. Mendonca, A. Campilho, Segmentation of retinal blood vessels by combining the detection of centerlines and morphological reconstruction, *IEEE transactions on medical imaging* 25 (9) (2006) 1200–1213.
- [75] K. BahadarKhan, A.A. Khaliq, M. Shahid, A morphological hessian based approach for retinal blood vessels segmentation and denoising using region based otsu thresholding, *PLoS one* 11 (7) (2016).
- [76] A.V. Oppenheim, R.W. Schaffer, *Digital Signal Processing*, Prentice-Hall, 1975.
- [77] H.G. Adelman, Butterworth equations for homomorphic filtering of images, *Computers in Biology and Medicine* 28 (28) (1998) 169–181.
- [78] R.C. Gonzales, P. Wintz, *Digital Signal Processing*, Addison-Wesley, 1987.
- [79] L.I. Voicu, H.R. Myler, A.R. Weeks, Practical considerations on color image enhancement using homomorphic filtering, *Journal of Electronic Imaging* 6 (1) (1997) 108–114.
- [80] S. Chaudhuri, S. Chatterjee, N. Katz, M. Nelson, M. Goldbaum, Detection of blood vessels in retinal images using two-dimensional matched filters, *IEEE Transactions on medical imaging* 8 (3) (1989) 263–269.
- [81] A.D. Fleming, S. Philip, K.A. Goatman, J.A. Olson, P.F. Sharp, Automated microaneurysm detection using local contrast normalization and local vessel detection, *IEEE transactions on medical imaging* 25 (9) (2006) 1223–1232.
- [82] T. Chanwimaluang, G. Fan, An efficient blood vessel detection algorithm for retinal images using local entropy thresholding, in: *Proceedings of the 2003 International Symposium on Circuits and Systems*, 2003. ISCAS'03., 5, IEEE, 2003. V–V.
- [83] E. Rodríguez-Esparza, L.A. Zanella-Calzada, D. Oliva, A.A. Heidari, D. Zaldivar, M. Pérez-Cisneros, L.K. Foong, An efficient harris hawks-inspired image segmentation method, *Expert Systems with Applications* (2020) 113428.
- [84] A.A. Heidari, S. Mirjalili, H. Faris, I. Aljarah, M. Mafarja, H. Chen, Harris hawks optimization: Algorithm and applications, *Future generation computer systems* 97 (2019) 849–872.
- [85] D. Oliva, S. Hinojosa, V. Osuna-Enciso, E. Cuevas, M. Pérez-Cisneros, G. Sanchez-Ante, Image segmentation by minimum cross entropy using evolutionary methods, *Soft Computing* 23 (2) (2019) 431–450.
- [86] M. Niemeijer, J. Staal, B. van Ginneken, M. Loog, M.D. Abramoff, Comparative study of retinal vessel segmentation methods on a new publicly available database, in: *Medical imaging 2004: image processing*, 5370, International Society for Optics and Photonics, 2004, pp. 648–656.
- [87] J. Zhang, Y. Chen, E. Bekkers, M. Wang, B. Dashtbozorg, B.M. ter Haar Romeny, Retinal vessel delineation using a brain-inspired wavelet transform and random forest, *Pattern Recognition* 69 (2017) 107–123.
- [88] A. Dasgupta, S. Singh, A fully convolutional neural network based structured prediction approach towards the retinal vessel segmentation, in: *2017 IEEE 14th International Symposium on Biomedical Imaging (ISBI 2017)*, IEEE, 2017, pp. 248–251.
- [89] Z. Fan, X. Yang, K.-T. Cheng, Joint segment-level and pixel-wise losses for deep learning based retinal vessel segmentation, *IEEE Transactions on Biomedical Engineering* 65 (9) (2018) 1912–1923.
- [90] S. Thangaraj, V. Periyasamy, R. Balaji, Retinal vessel segmentation using neural network, *IET Image Processing* 12 (5) (2017) 669–678.
- [91] Y. Guo, Ü. Budak, A. Şengür, A novel retinal vessel detection approach based on multiple deep convolution neural networks, *Computer methods and programs in biomedicine* 167 (2018) 43–48.
- [92] J. Zhang, B. Dashtbozorg, E. Bekkers, J.P. Pluim, R. Duits, B.M. ter Haar Romeny, Robust retinal vessel segmentation via locally adaptive derivative frames in orientation scores, *IEEE transactions on medical imaging* 35 (12) (2016) 2631–2644.
- [93] M. Shahid, I.A. Taj, Robust retinal vessel segmentation using vessel's location map and frangi enhancement filter, *IET Image Processing* 12 (4) (2018) 494–501.
- [94] Z. Fan, J. Lu, C. Wei, H. Huang, X. Cai, X. Chen, A hierarchical image matting model for blood vessel segmentation in fundus images, *IEEE Transactions on Image Processing* 28 (5) (2018) 2367–2377.
- [95] H. Aguirre-Ramos, J.G. Avina-Cervantes, I. Cruz-Aceves, J. Ruiz-Pinales, S. Ledesma, Blood vessel segmentation in retinal fundus images using gabor filters, fractional derivatives, and expectation maximization, *Applied Mathematics and Computation* 339 (2018) 568–587.

- [96] M.B. Abdallah, A.T. Azar, H. Guedri, J. Malek, H. Belmabrouk, Noise-estimation-based anisotropic diffusion approach for retinal blood vessel segmentation, *Neural Computing and Applications* 29 (8) (2018) 159–180.
- [97] S. Pal, S. Chatterjee, D. Dey, S. Munshi, Morphological operations with iterative rotation of structuring elements for segmentation of retinal vessel structures, *Multidimensional Systems and Signal Processing* 30 (1) (2019) 373–389.
- [98] K. Yue, B. Zou, Z. Chen, Q. Liu, Improved multi-scale line detection method for retinal blood vessel segmentation, *IET Image Processing* 12 (8) (2018) 1450–1457.
- [99] B. Biswal, T. Pooja, N.B. Subrahmanyam, Robust retinal blood vessel segmentation using line detectors with multiple masks, *IET Image Processing* 12 (3) (2017) 389–399.
- [100] S. Roy, A. Mitra, S. Roy, S.K. Setua, Blood vessel segmentation of retinal image using clifford matched filter and clifford convolution, *Multimedia Tools and Applications* 78 (24) (2019) 34839–34865.